On the distribution of the the near-solar bound dust grains detected with Parker Solar Probe

S. Kočiščák[1],[⋆], A. Theodorsen[1], and I. Mann[1]

Department of Physics and Technology, UiT The Arctic University of Norway, 9037, Tromsø, Norway

ABSTRACT

Context. Parker Solar Probe (PSP) counts dust impacts in the near-solar region, but modelling effort is needed to understand the dust population's properties.
Aims. First, we formulate questions which rise upon the data inspection and upon the comparison of the PSP data with the closest different measurement, that is the dust count provided by Solar Orbiter (SolO). We build a parametric forward-model for the bound dust detection rates in the near-solar environment to confront the data with different assumptions.
Methods. We derive the 6D pahse space distribution of the dust in a reasonably general form. We apply the model in this general form to the location table of different PSP's solar encounter groups. We explain some of the near-perihelion features observed in the data as well as the broader characteristic of the dust flux inside 0.5 AU.
Results. We found indication that the heat shield of PSP is less sensitive to the dust impacts, compared to the other PSP's surfaces. We propose that the heat shield becoming conductively coupled to the spacecraft body near the Sun is possibly related to the steep change in the spacecraft's potential near the Sun. We found that the dust flux observed in the post-perihelia within 0.5 AU are consistent with a broad range of orbital parameters, including circular dust, but the scaling of the dust number density with heliocentric distance and the scaling of detection efficiency with the relative speed are very important to explain the observed dependence, but the latter is likely lower than previously assumed. Regarding the near-perihelion flux, we report that the observed locations of flux maxima are not consistent with the locations predicted by the circular dust model, yet the position depends on the assumed flux scaling with velocity. Other studied parameters are not found capable of moving the predicted maxima outwards.
Conclusions. We show that the post-perihelion flux can be explained by non-circular bound dust in combination with the detection capabilities of PSP, and that the scaling of flux with the impact speed is especially important.

Key words. cosmic dust – Parker Soalr Probe – phase-space distribution

1. Introduction

1.1. Dust on Parker Solar Probe

Parker Solar Probe (*PSP*), which orbits the Sun on an eccentric orbit between 0.05 AU and 1 AU was found to be sensitive to dust impacts (Szalay et al. 2020; Malaspina et al. 2020; Page et al. 2020) thought the fast electrical measurements of its FIELDS suite (Bale et al. 2016). The innermost solar system region is a very dusty environment, and in addition to the electrical antennas, dust phenomena were observed with the Wide-Field Imager for Parker Solar Probe (*WISPR*) (Stenborg et al. 2021; Malaspina et al. 2022) and dust possibly damaged the Integrated Science Investigation of the Sun (*IS⊙IS*) (Szalay et al. 2020).

It was found that the dust detection can be successfully modelled as a combination of bound and hyperbolic dust, so-called β meteoroids (Szalay et al. 2021). During the initial orbits, most impacts were attributed to β meteoroids. However, during the later orbits, and especially as the perihelia got inside the β meteoroid creation region (Malaspina et al. 2020) and in postperihelia, where the relative speed between β meteoroids and the PSP is low, the dust count are likely to sometimes be dominated by bound dust.

Szalay et al. (2021) observed a clear double peak structure with a minimum in perihelion during the orbits 4, 5, and 6 of

⋆ samuel.kociscak@uit.no

PSP. The minimum was anticipated and at least partially explained by Szalay et al. (2020) as being due to alignment between the nearly-circular speed of bound dust and purely azimuthal speed of PSP in the perihelion. Szalay et al. (2021) also explained the post-perihelion maximum as being potentially due to the encounter between PSP and the hypothesized Geminids β-streamer produced by the collisional griding between the zodiacal cloud and the Gemminids meteoroid stream.

1.2. Data

In the present work, we use the data of detected dust counts along the trajectory of PSP made available by Malaspina et al. (2023). The data are built on the TDSmax data product of the FIELDS instrument, and assume that all the fast electrical phenomena strong enough in the monopole measurement detected over quiet enough periods of time contain dust impacts. This was demonstrated to be a good approximation of the actual dust count, with about 10.5 % false positive rate and about 7 % miss rate (Malaspina et al. 2023). The data is structured in intervals of 8 h, and contains the impact count in the time interval corrected for under-counting, as well as the total effective observation time in the 8 h interval, corrected for the time then wave activity made dust detection ineffective. Detailed description of the data product is available in Malaspina et al. (2023).

1.3. PSP vs SolO

PSP's observations of the inner zodiacal cloud are unique, and the closest available comparable observations are those of Solar Orbiter (SolO) (Mann et al. 2019). Compared to PSP, Solo experiences much lower radial speed, doesn't go nearly as close to the Sun, and the dust flux it measures is always dominated by β-meteoroids (Zaslavsky et al. 2021). Those were concluded to have the diameter of $d \gtrsim 100$ nm (Zaslavsky et al. 2021) and $\beta \gtrsim 0.5$ (Kočiščák et al. 2023). PSP however observes a significant amount of bound dust grains, which are much larger, at $d \gtrsim 1 \mu m$. The detection is carried out by rigid cylindrical antennas near the heat shield for both spacecraft, with an important difference between the heat shields. While both spacecraft are protected against the extreme near-solar conditions by a heat-shield, the front-side of SolO's heat shield is made of titanium and is conductively coupled to the rest of the spacecraft body (Damasio et al. 2015), while the PSP's heat shield is neither (Reynolds et al. 2013; Diaz-Aguado et al. 2021).

A model for the β-meteoroid flux observed by both spacecraft must be currently built on many assumptions, as there are many unknowns to the population of β-meteoroids. Any differences between the fluxes might be attributed to the properties of the population, or to the differences between the two spacecraft, which are numerous. The population was studied extensively by these (Szalay et al. 2021; Zaslavsky et al. 2021; Kočiščák et al. 2023) and by other spacecraft (Zaslavsky et al. 2012; Malaspina et al. 2014) and is out of focus of the present work, which focuses on the bound dust. Constraining the bound dust component will however provide information on β-meteoroids, since they together make up the detected flux.

1.4. Aim of the work

For the purpose of this work, we focus on the post-perihelion data of each orbit. There are two reasons for this: first, we want to focus on the bound dust, not the β meteoroids, and second, the front side of the Thermal Protection System's heat shield (*TPS*) of PSP is believed to be less sensitive to dust impacts, compared to other surfaces of the spacecraft. Both these support the validity of the assumption that in the right region in post-perihelia, the observed flux can be explained with only bound dust.

1.4.1. Bound dust and β meteoroids

One of the difficulties in explaining the observed flux is that several populations contribute to the detections (Szalay et al. 2020, 2021; Kočiščák et al. 2023), and therefore several components of the impact rate must be assumed, which greatly decreases the fidelity of parameter estimation. As was debated and demonstrated previously, the main contributors to the dust detections done by PSP are bound and β meteoroids. Bound dust grains are in orbits, and therefore have both positive and negative heliocentric speeds. Since β meteoroids are on outbound trajectories, each of them has a positive heliocentric speed, and therefore, the proportion of impacts of bound dust to all impacts is the highest when PSP's radial speed is significant. The relative speed between PSP and bound dust than between PSP and β meteoroids was studied by Szalay et al. (2020). Under the assumption of perfectly circular bound dust trajectories with $\beta = 0$ and β meteoroids originating at $R_0 = 5 R_{sun}$ and having $\beta = 0.5$, the relative speed between PSP and bound dust was found by Szalay et al. to be higher at 0.15 AU $< R < 0.5$ AU for the 6th and subsequent orbits. A two-component fit to the data performed by (Szalay

et al. 2021) is consistent with the flux of bound dust being higher than the flux of β for 0.15 AU $< R < 0.5$ AU during the 6th orbit. In fact, the fit suggests that bound dust flux is more than a decade lower than in β meteoroid flux for the 6th perihelion's outbound leg at $R = 0.2$ AU. Although the exact numbers and distances are model specific, the general trend is clear, that the bound dust flux is higher than β meteoroid flux for a good portion of the post-perihelion passage for all the PSP's later orbits.

1.5. Thermal Protection System

A crucial component of the PSP's Thermal Protection System (TPS), the heat shield, consists of alumina coated carbon-carbon in from of carbon foam (Reynolds et al. 2013). Since the front side of the heat shield is non-conductive, it is not on the same potential as the rest of the spacecraft. The front side only becomes conductively coupled to the spacecraft body through plasma currents, once the spacecraft is inside ≈ 0.16 AU (Diaz-Aguado et al. 2021). The heat shield is exposed to dust impacts and impacts on the heat shield generate impact plasma (Shen 2021), which is potentially identified in the antenna measurements. Unlike impacts in the spacecraft parts connected conductively with the body ground, impacts on the heat shield only produce dipole response, which is more directionally dependent (Shen et al. 2023) and generally weaker (Mann et al. 2019). Moreover, the amount of charge generated by impacts on the heat-shield is comparably lower, with respect to other common spacecraft materials, see Fig. 1.
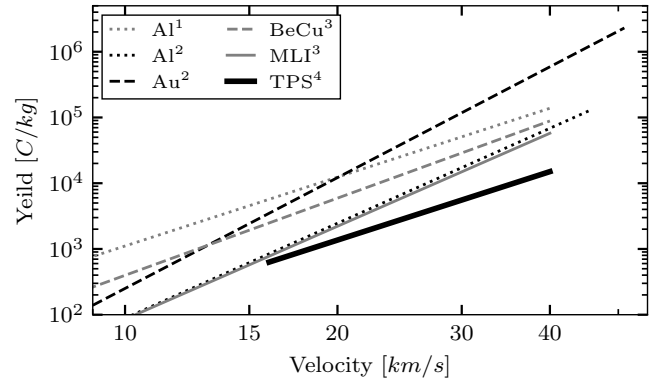

Fig. 1: Mass-normalized impact charge yield for several common spacecraft materials, assuming 10^{-14} kg dust. TPS stands for PSP's Thermal Protection System and MLI stands for the multilayer insulation of Solar Terretrial Relations Observatory (STEREO). References: 1 – McBride & McDonnell (1999), 2 – Grün (1984), 3 – Collette et al. (2014), 4 – Shen (2021). All experiments were done with iron grains.

In order to investigate the heat shield's sensitivity using the data, we study near orbital alignments between SolO and PSP. Although these have very different final orbits, earlier PSP orbits resemble later SolO orbits in terms of velocities and orbital speeds. Six nearest such alignments were found and are listed in Tab. 1. Three of these are in pre-perihelion ($v_r < 0$) and three are in post-perihelion ($v_r > 0$). When the radial speed $v_r < 0$, the ram-direction of the spacecraft is in front of the spacecraft and the proportion of impacts on the heat shield is likely higher, than in the case when the radial speed $v_r > 0$ and the ram-direction is behind the spacecraft. Under the assumption of a lower heat-

shield detection effectiveness for PSP, the more homogeneous SolO with a conductive heat shield should detect relatively more dust, when $v_r < 0$. The indication of this is observed in comparison of the flux during the six alignments in Fig. 2. The lower sensitivity of the PSP's heat shield is consequential for evaluating the bound and β dust properties.
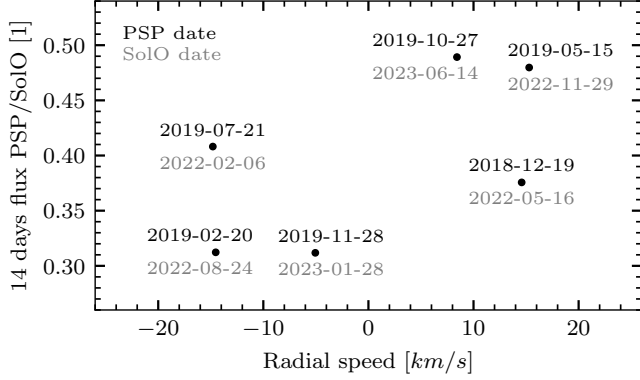

Fig. 2: Comparison of the 14 days cumulative flux (centered at the indicated day) observed with PSP and with SolO during their near alignments. A positive correlation is observed. See Tab. 1 for the orbital speeds corresponding to the individual points.

1.6. PSP potential

The potential of the spacecraft was shown to be consequential for the dust detection (Shen et al. 2023). In the absence of a more reliable measurement, the floating potential of PSP can be estimated as the average of the DC voltages V_i between the antenna i and the spacecraft (Bale et al. 2020). If the antennas are on the local plasma potential, then the antennas measure voltage between the spacecraft body and the ambient plasma. Time points were drawn uniformly randomly from the first 30 months of the mission and the potential was inferred this way using DFB_WF_DC data product of *FIELDS* (Malaspina et al. 2016). The dependence of the spacecraft potential on the heliocentric distance is shown in Fig. 3. It is observed that the potential is mostly positive outside of 0.3 AU, close to zero at around 0.2 AU, and changing suddenly inward of 0.15 AU. This is merely an approximation of the spacecraft potential, there are many factors beyond the heliocentric distance, which influence the final potential (Guillemant et al. 2012, 2013), and the potential of the TPS heat shield is presumably different again, since its front side is not conductively coupled to the spacecraft, as discussed in Sec. 1.5. Nevertheless, this analysis serves as a probe into the state of the spacecraft and a cautious conclusion is drawn that the dust detection process does not change significantly with the heliocentric distance, if the spacecraft is outside of 0.15 AU. This distance is similar to the distance of ≈ 0.16 AU, inside which the heat shield becomes conductively coupled to the spacecraft body (Diaz-Aguado et al. 2021), and these two are both relevant for the dust detection effectiveness, and are possibly related.

1.7. Description of the model

We present a parametric model for bound dust detections on a spacecraft. The model is partially build using the formalism of 6D distribution function over space x and velocity v: $f(x, v) =$
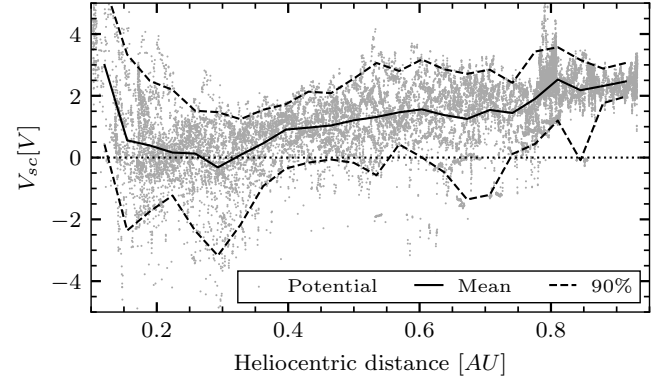

Fig. 3: Spacecraft potential estimated as the average of four *DC* antenna measurements.

$f(x_1, x_2, x_3, v_1, v_2, v_3)$, similarly to how this is done in plasma theory. A single population of dust gravitationally bound to the Sun is assumed. The dust number density $n(r)$ is evaluated as

$$n(\boldsymbol{r}) = \iiint_{\mathbb{R}^3} f(x, y, z, v_x, v_y, v_z) \, dv_x \, dv_y \, dv_z, \tag{1}$$

where the unit of n is $[n] = m^{-3}$. The flux $j(r)$ as perceived by the spacecraft is evaluated as the first moment of relative speed between the spacecraft and the dust. For example, the flux through a stationary test loop oriented perpendicular to the x-axis is

$$j_x(\boldsymbol{r}) = \iiint_{\mathbb{R}^3} |v_x| f(x, y, z, v_x, v_y, v_z) \, dv_x \, dv_y \, dv_z, \tag{2}$$

where the unit of j_x is $[n] = m^{-3} s^{-1}$. The model does not natively work with masses, and merely assumes all the dust grains are detected on contact with the spacecraft, regardless of the impact speed v_{impact} or grain's mass m. The focus of the model is not to explain the absolute amount of the detected dust, the model works with a multiplicative prefactor.

The model captures dust's eccentricity e, inclination θ, radiation pressure to gravity ratio β, and the fraction of retrograde dust grains in the population rp. The spatial scaling of density $n(r)$ is assumed spherically symmetric:

$$n(\boldsymbol{r}) \propto r^\gamma, \tag{3}$$

which allows the presented study of γ. The model can be modified to cylindrical symmetry by assuming dependence on the distance from the plane of ecliptics, yet this is out of scope of this work, since the spacecraft of interest operate very close to the plane of ecliptics. The model is capable of capturing dependence of the flux through the surface i, denoted j_i on impact speed by evaluating a moment different from $|v_{impact}|$. In this work, we assume the dependence

$$j_i \propto v_{impact}^\epsilon, \tag{4}$$

where ϵ is equivalent to $1 + \alpha\delta$ as used in several publications (Szalay et al. 2021; Zaslavsky et al. 2021; Kočiščák et al. 2023). The model treats all the parameters $e; \theta; \beta; rp; \gamma; \epsilon$ as single values (degenerate distributions), which can be, owing to the linearity, generalized to a sum of terms approximating an arbitrary distribution of these parameters, but this is mostly out of scope of present work. The model might in principle deal with an arbitrary shape of the spacecraft, but since the spacecraft of interest

Table 1: Near alignments of speed and heliocentric distance between PSP and SolO.

PSP date	R[AU]	v_r[km/s]	v_ϕ[km/s]	SolO date	R[AU]	v_r[km/s]	v_ϕ[km/s]
27/10/2019	0.886	7.9	17.7	14/06/2023	0.878	8.9	22.5
28/11/2019	0.911	−5.1	17.3	28/01/2023	0.928	−5.0	21.6
19/12/2018	0.785	15.4	19.9	16/05/2022	0.821	13.8	25.1
20/02/2019	0.785	−15.45	20.2	24/08/2022	0.822	−13.7	25.7
21/07/2019	0.779	−15.75	20.4	06/02/2022	0.818	−13.9	25.9
15/05/2019	0.760	16.85	20.6	29/11/2022	0.785	13.8	25.1

is PSP, cylindrical shape, with the axis pointing towards the Sun, is assumed.

The most important component of the model is the 6D distribution function f, which is derived to be in the shape

$$f(x, y, z, v_x, v_y, v_z) = C \cdot (rv_\phi)^\gamma \delta(z)\delta(v_z)\delta\left(v_r \pm \tilde{v}\right), \quad (5)$$

where

$$\tilde{v} = \frac{\sqrt{(e^2 - 1)\mu^2 + 2\mu v_\phi^2 r - v_\phi^4 r^2}}{v_\phi r}, \quad (6)$$

which is Eq. A.31 of Appendix A. The independent integration variable for the moments of f (such as Eq. 2) is chosen to be the dust azimuthal speed v_ϕ, and the inegration boundaries are then the lowermost and the highermost speeds the dust grains might have, given their eccentricity e and the effective gravity $\mu(\beta)$, therefore

$$\sqrt{\frac{(1-e)\mu}{r}} < v_\phi < \sqrt{\frac{(1+e)\mu}{r}}, \quad (7)$$

which is Eq. A.34 of Appendix A. The derivation of the equations and further discussion of the model is in Appendix A.

Practically, the model evaluates the flux on the spacecraft, given the position and the speed of the spacecraft, and is therefore straight-forward to use the model to generate flux profiles starting with a position table of the spacecraft of interest, which is presently PSP.

2. Scaling of the flux with distance

One of the features which the model should reproduce is the macroscopic scaling of the observed flux with the heliocentric distance. In this section, we compare the model results to the data in the region, where the flux is dominated by bound dust impacts.

Inspection of the data shows that, with the exception of the first orbital group, which has its perihelion outside of 0.15 AU, the flux scales approximately as $j \propto R^{-2.5}$ over the outbound leg of each orbit between 0.15 AU and 0.5 AU. This is shown in Fig. 4.

The model is applied to a representative orbit from each of the encounter groups. These are described in Appendix B. The base model is considered: $e = 0; \theta = 0; rp = 0; \beta = 0; \gamma = -1.3; \epsilon = 1$, which is in line with the assumptions of particles on circular orbits, no inclination, no radiation pressure, no retrograde grains, spatial number density scaling as $n \propto R^{-1.3}$ and the assumption that every grain is always detected, if impact happened: $j \propto v_{impact}$. It is found that these assumptions are not compatible (Fig. 5) with the slope observed in the data (Fig. 4), since the dependence produced by the model is appreciably shallower than $\propto R^{-2.5}$.
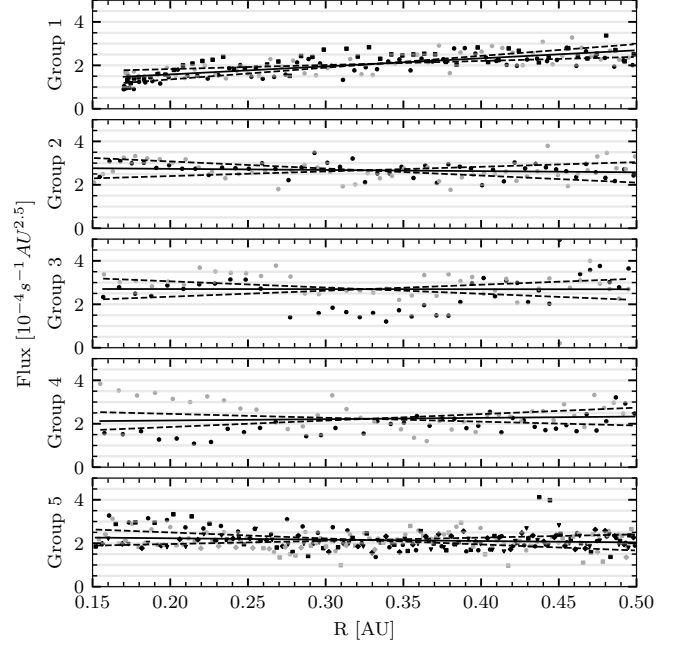

Fig. 4: The flux as detected by PSP in the outbound part of each orbit, compensated by $R^{-2.5}$, grouped by orbital groups. Individual encounters within a group are distinguished by markers of different shape or color. The solid lines are the linear fits to the compensated flux. The dashed lines are the fits of the data, if compensated by $R^{-2.2}$ and $R^{-2.8}$, to demonstrate the approximate accuracy of the $R^{-2.5}$ scaling.

It is found that the parameters $e; \theta; \beta; rp$ all influence the slope in the right direction (see Appendix C), yet even in the most favorable case, they do not suffice to explain the slope observed in the data, as is shown in Fig. 5. It is also seen from Fig. 5 that especially the flux during the later orbits is very little influenced by these four parameters. The explanation, therefore, lies at least partially in the scaling of density with heliocentric distance γ and the scaling of flux with the relative speed ϵ. These both influence the slope appreciably, as is seen in Figs. 7 and 8. We see that in the most unfavourable case of all the other parameters being equal to the base value, $\gamma \approx 3$, resp. $\epsilon \approx -3$ show nearly flat plots, and, therefore, serve as upper estimates of the values. Many combinations of the 6 parameters are capable of reproducing the right slope, and arguing for the most likely combination is beyond the scope of this work, since the model is likely not sufficient, as it assumes constant parameters. A viable combination of parameters is shown in Fig. 9, but we note that the slope is not very sensitive to changes in $e; \theta; \beta; rp$. Viable combinations of the most influential parameters: γ and ϵ are shown in Fig. 6, where the other four parameters are included
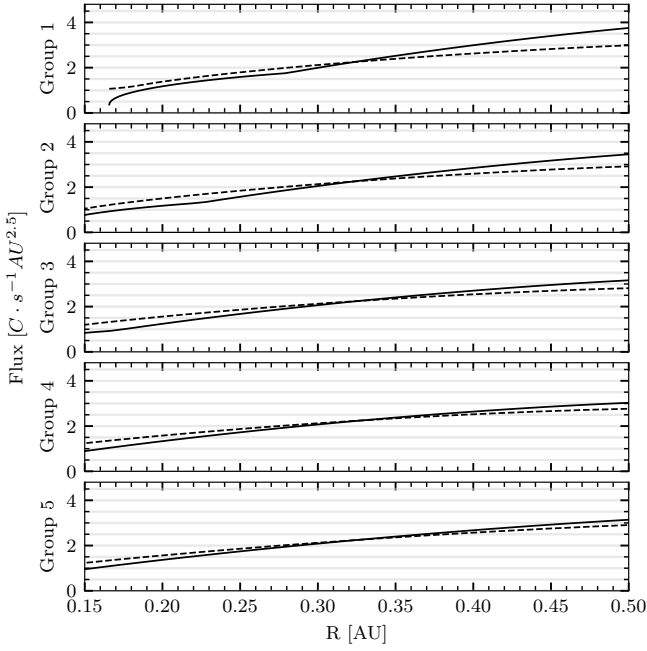
Fig. 5: The base model-predicted flux is shown in the solid line, compensated by $R^{-2.5}$. The slope is considerably shallower than $\propto R^{-2.5}$, hence the inclining trend after the compensation. The model-predicted flux in the case of $e = 0.5; \theta = 45°; rp = 10\%; \beta = 0.5; \gamma = -1.3; \epsilon = 1$ is shown in the dashed line. Even these, rather extreme, assumptions don't suffice to explain the slope observed in the data.

together in two cases: the base case, and the upper estimate: the dashed case from Fig. 5.
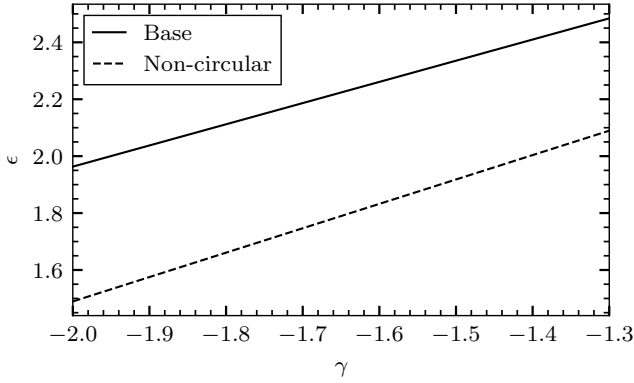
Fig. 6: The combinations of γ and ϵ, which produce the profile, which approximately matches the slope of -2.5. The base model assumes $e = 0; \theta = 0; rp = 0; \beta = 0$ and the non-circular model assumes rather extreme $e = 0.5; \theta = 45°; rp = 0.1; \beta = 0.5$.

3. Near-sun profile

The model is capable of reproducing features observed in the data close to perihelia. Notably, there is a distinct minimum in the flux observed in the perihelion. This minimum was attributed to the velocity alignment between PSP and bound dust (Szalay
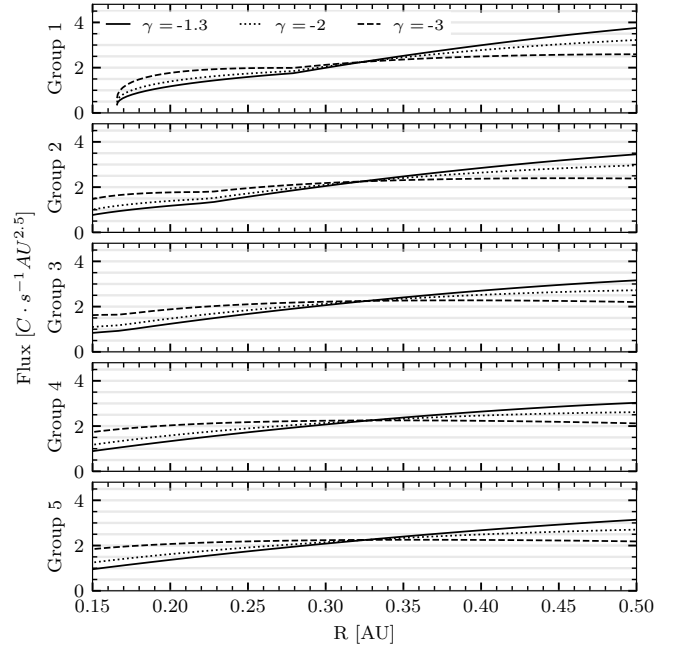

Fig. 7: The base model-predicted flux is shown in the solid line. In addition, the influence of the heliocentric distance scaling γ on the slope is demonstrated.
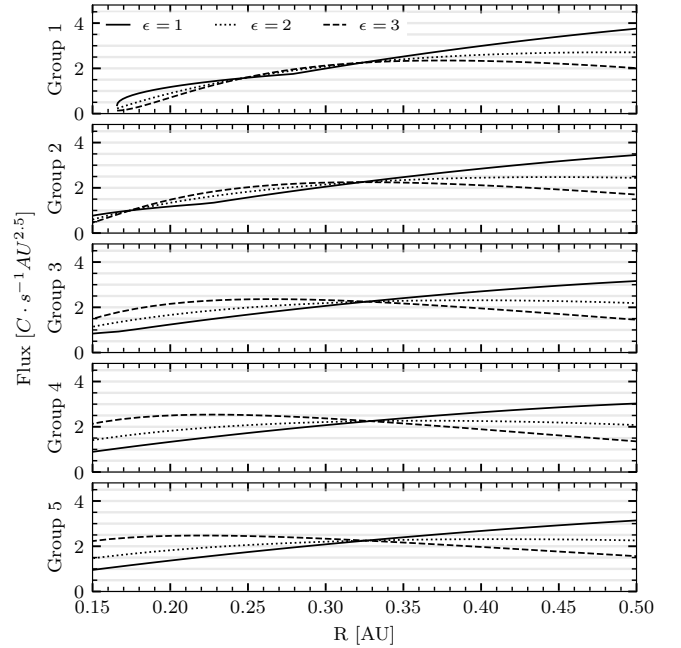

Fig. 8: The base model-predicted flux is shown in the solid line. In addition, the influence of the velocity exponent ϵ on the slope is demonstrated.

et al. 2021). In this section, the near-solar flux is studied as a function of the free parameters of the model.

The observational data is shown in Fig. 10 and the near-perihelion minimum is apparent. We note that the flux is not symmetric around the perihelia, the reasons for this are discussed in Secs. 1.4.1 and 1.5. We focus on the post-perihelia, as we will seek the consistency between these and the model predictions.
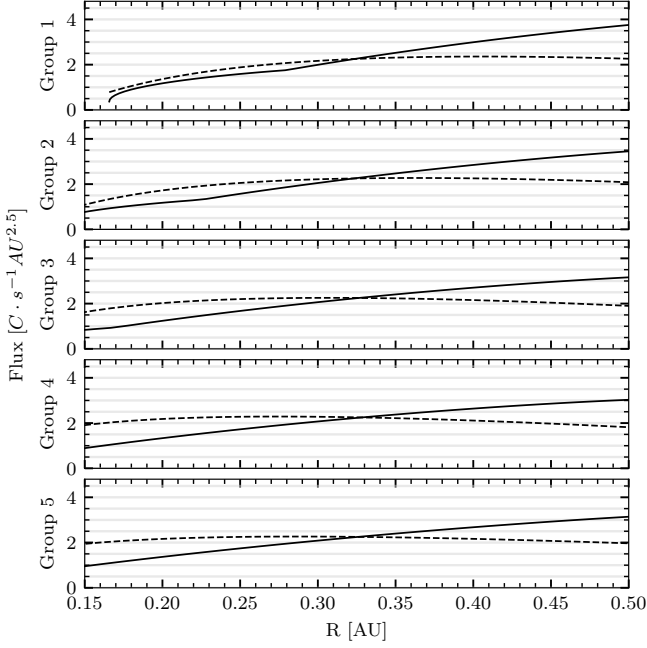
Fig. 9: The base model-predicted flux is shown in the solid line. In addition, the model with parameters: $e = 0.1; \theta = 10°; rp = 0.03; \beta = 0.05; \gamma = -1.9; \epsilon = 2$ is shown as a representative of a viable option.
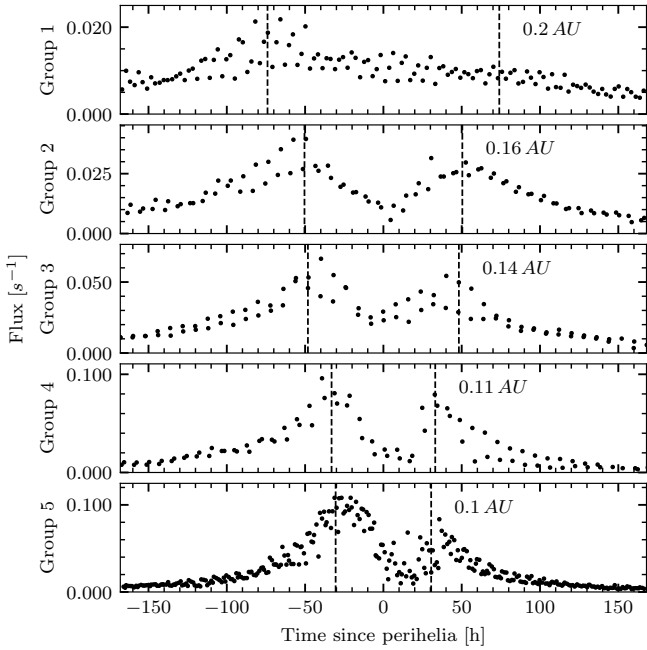

Fig. 10: The detection rate of dust impacts near the perihelia. The data from individual solar encounters are grouped according to the orbital groups.

The model-predicted flux is shown in Fig. 11 and we note it is symmetric around the perihelia: since only the bound dust population is assumed, and the heat shield is assumed as sensitive as the rest of the spacecraft, there is nothing to cause the asymmetry. The same set of vertical lines, approximately corresponding to the heliocentric locations of the maxima are shown

symmetric around the perihelia in Figs. 10 and 11. There is no post-perihelion maximum in orbital group 1, the vertical line is based solely on the pre-perihelion maximum. In case of the base model (as before, $e = 0; \theta = 0; rp = 0; \beta = 0; \gamma = -1.3; \epsilon = 1$), the maxima in the flux are predicted decidedly closer to the perihelia than observed. It is observed in the same figure that by varying the velocity exponent ϵ the location of the expected maxima is moved, possibly to the extent that it is consistent with the data. None of the other parameters influences the location of the maxima of the flux appreciably and they are shown and discussed in App. D. They however do influence the relative depth of the near-perihelion flux minimum. Increasing any value except for the velocity exponent ϵ would result in a shallower perihelion dip, see the comparison on the influence of each individual parameter in App. D.
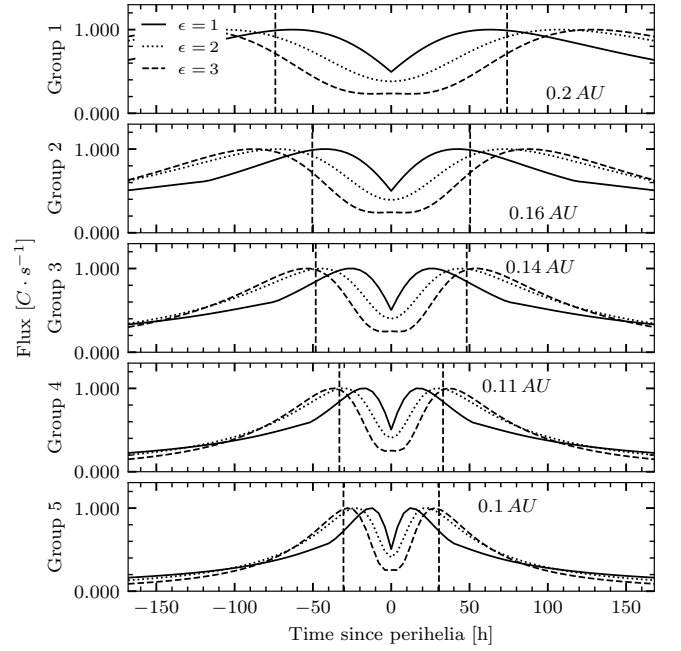

Fig. 11: The base model-predicted flux near the perihelia is shown in solid line. Different values of ϵ are shown for comparison. The same vertical dashed lines as in Fig. 10 are shown for reference.

Fig. 12 shows the same combination of parameters as Fig. 9 does, which was found reasonable and viable to explain the observed post-perihelion slope. Even in this reasonably conservative parameter choice, the perihelion dip is nearly gone, due to a much worse alignment between the spacecraft's and the dust's speed. It is also observed that ϵ is a lot less effective at changing the position of the maxima, if other parameters are higher than in the base model. We conclude that it is unlikely that the near perihelion dip is solely due to the velocity alignment between the dust cloud and the spacecraft.

4. Discussion

The two lines of $\epsilon(\gamma)$ in Fig. 6 may be regarded as an upper and a lower estimate of ϵ. It is therefore found that the velocity exponent ϵ lies between 1.5 and 2.5, assuming the other parameters reasonable. This is much lower then previously assumed 4.15 (Szalay et al. 2021) and might indicate that the assumption
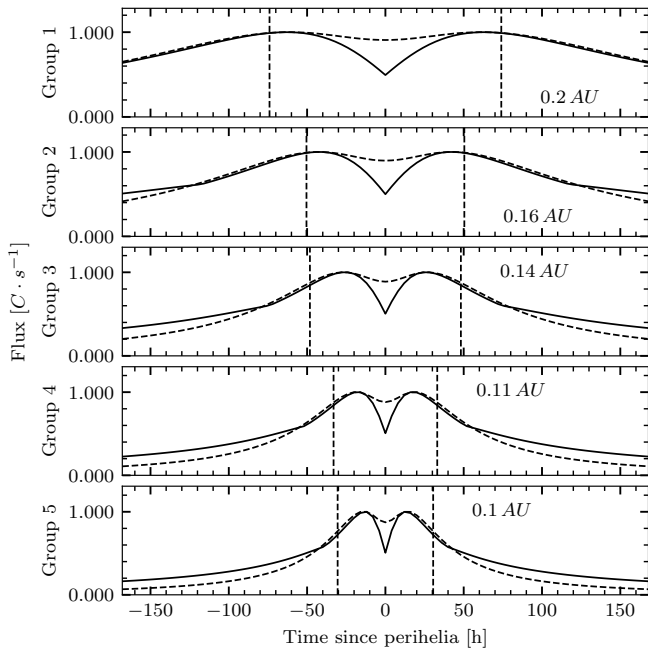
Fig. 12: The base model-predicted flux near the perihelia is shown in solid line. In addition, the model with parameters: $e = 0.1; \theta = 10°; rp = 0.03; \beta = 0.05; \gamma = -1.9; \epsilon = 2$ is shown as a representative of a viable option.

of the flux j_i scaling with a power of velocity v (Eq. 4) is not justified for bound dust.

If the near perihelion dip is not due to the velocity alignment, other options are available, and we list three of them. First, the number density of the dust is believed to slowly diminish as the spacecraft probes closer to the Sun, as the dust depletion zone (DDZ) and the dust free zone (DFZ) were hypothesised to exist (Russell 1929), since the dust grains erode rapidly in the near solar extreme conditions. It was estimated using WISPR that DDZ lies inward of $19\,R_{sun} \approx 0.09$ AU and DFZ likely lies inward of $5\,R_{sun} \approx 0.023$ AU. Therefore, this partially explains the apparent depletion of dust near the perihelion. The second available explanation of the dip might lie in ineffective detection. The antenna detection process is very much dependent on the spacecraft's state, and the environment (Shen et al. 2021; Racković Babić et al. 2022; Shen et al. 2023). An indication that the process changes rapidly inward of 0.2 AU is that the spacecraft's potential seems to be a steep function of the heliocentric distance in this region, potentially disturbing the otherwise effective dust detection routines. For example, the heat shield becoming conductively coupled to the spacecraft's body inward of ≈ 0.16 AU also changes spacecraft's state. See Sec. 1.6 for the discussion of the spacecraft potential. The third available explanation is that as the relative speed between the dust and the spacecraft is higher than a certain threshold, all the present dust grains are detected, and therefore the proportionality of flux to $\propto v^\epsilon$ is no longer the case. This would not produce the dip on its own, but leads to a relative depletion with respect to the case, when the proportionality of flux to $\propto v^\epsilon$ is assumed all the way. We also note that the apparent under-counting near the perihelia might be enhanced by a possible over-counting before and after each of the perihelia, as the spacecraft might even get more sensitive to dust impacts, possibly due to a higher potential (Fig. 3) and / or better than elsewhere sensitivity of the heat shield in the region.

5. Conclusions

The dust detection counts recorded on PSP suggest that PSP's the heat shield (PSP/TPS) offers a less dust sensitive target, compared to the heat shield of SolO and to the other common spacecraft materials. This might be causally related to the sudden change of the spacecraft potential inside 0.15 AU.

We developed a model for bound dust flux, which takes into account non-zero values of physical dust parameters: eccentricity e, inclination i, radiation pressure to gravity ratio β, and retrograde dust fraction rp. In addition, the model takes into account semi-empirical parameters: the number density dependence on the heliocentric distance γ and the detection rate dependence on the impact speed ϵ.

The model was used to demonstrate the influence of the free, and in reality poorly constrained, parameters on the dependence of the dust detection rate on the heliocentric distance. This dependence seemingly follows a power-law in the post-perihelion region, where the influence of β dust is expected the lowest. It was found that the physical parameters of the dust: e, i, β, rp all have minor influence on the power-law slope, while the semi-empirical parameters γ and ϵ are crucial, and can explain the observed slope. The velocity exponent ϵ is found to likely be between 1.5 and 2.5, which is lower than previously assumed.

The dust detection counts near the perihelia of PSP were studied and compared to the model results. We found that the perihelion dip observed in the data is hard to reproduce with reasonable values of the free parameters in the model. The locations of the maxima in the model are found much closer to the perihelia than in reality. The dip is found much shallower in the model than in reality. This suggests that other effects are responsible for the perihelion dip, beyond the velocity alignment between the spacecraft and bound dust. Dust depletion zone, variable spacecraft conditions, and the saturation in the dust threshold size are introduced as possibilities.

References

Bale, S., Goetz, K., Bonnell, J., et al. 2020, arXiv preprint arXiv:2006.00776

Bale, S., Goetz, K., Harvey, P., et al. 2016, Space science reviews, 204, 49

Collette, A., Grün, E., Malaspina, D., & Sternovsky, Z. 2014, Journal of Geophysical Research: Space Physics, 119, 6019

Damasio, C., Defilippis, P., Draper, C., & Wild, D. 2015, in 45th International Conference on Environmental Systems ICES–2015-7612-1, Vol. 6

Diaz-Aguado, M., Bonnell, J., Bale, S., Wang, J., & Gruntman, M. 2021, Journal of Geophysical Research: Space Physics, 126, e2020JA028688

Giese, R., Kneissel, B., & Rittich, U. 1986, Icarus, 68, 395

Grün, E. 1984, The Giotto Spacecraft Impact-induced Plasma Environment, 39

Guillemant, S., Génot, V., Matéo-Vélez, J.-C., Ergun, R., & Louarn, P. 2012, 30, 1075

Guillemant, S., Génot, V., Velez, J.-C. M., et al. 2013, IEEE Transactions on Plasma Science, 41, 3338

Kočiščák, S., Kvammen, A., Mann, I., et al. 2023, Astronomy & Astrophysics, 670, A140

Malaspina, D., Horányi, M., Zaslavsky, A., et al. 2014, Geophysical Research Letters, 41, 266

Malaspina, D. M., Ergun, R. E., Bolton, M., et al. 2016, Journal of Geophysical Research: Space Physics, 121, 5088

Malaspina, D. M., Stenborg, G., Mehoke, D., et al. 2022, The Astrophysical Journal, 925, 27

Malaspina, D. M., Szalay, J. R., Pokornỳ, P., et al. 2020, The Astrophysical Journal, 892, 115

Malaspina, D. M., Toma, A., Szalay, J. R., et al. 2023, The Astrophysical Journal Supplement Series, 266, 21

Mann, I., Nouzak, L., Vaverka, J., et al. 2019, Annales Geophysicae, 37, 1121

McBride, N. & McDonnell, J. 1999, Planetary and Space Science, 47, 1005

Page, B., Bale, S. D., Bonnell, J., et al. 2020, The Astrophysical Journal Supplement Series, 246, 51

Racković Babić, K., Zaslavsky, A., Issautier, K., Meyer-Vernet, N., & Onic, D. 2022, Astronomy & Astrophysics, 659, A15

Reynolds, E. L., Driesman, A., Kinnison, J., & Lockwood, M. K. 2013, in AIAA Guidance, Navigation, and Control (GNC) Conference, 4879

Russell, H. N. 1929, Astrophysical Journal, vol. 69, p. 49, 69, 49

Shen, M.-H. 2021, PhD thesis, University of Colorado at Boulder

Shen, M. M., Sternovsky, Z., Garzelli, A., & Malaspina, D. M. 2021, Journal of Geophysical Research: Space Physics, 126, e2021JA029645

Shen, M. M., Sternovsky, Z., & Malaspina, D. M. 2023, Journal of Geophysical Research: Space Physics, 128, e2022JA030981

Stenborg, G., Howard, R., Hess, P., & Gallagher, B. 2021, Astronomy & Astrophysics, 650, A28

Szalay, J., Pokornỳ, P., Bale, S., et al. 2020, The Astrophysical Journal Supplement Series, 246, 27

Szalay, J., Pokorný, P., Malaspina, D., et al. 2021, The Planetary Science Journal, 2, 185

Zaslavsky, A., Mann, I., Soucek, J., et al. 2021, Astronomy & Astrophysics, 656, A30

Zaslavsky, A., Meyer-Vernet, N., Mann, I., et al. 2012, Journal of Geophysical Research: Space Physics, 117

Appendix A: Integrating the pahse-space density

Appendix A.1: Pahse-space density

Assume there is a time-invariant dust density f in the usual 6D phase space:

$$f(\mathbf{r}, \mathbf{v}) = f(x, y, z, v_x, v_y, v_z), \tag{A.1}$$

which is normalized to number density as

$$n(x, y, z) = \iiint_{\mathbb{R}^3} f(x, y, z, v_x, v_y, v_z)\, dv_x\, dv_y\, dv_z, \tag{A.2}$$

which is a very useful way of looking at it, since $n(\mathbf{r})$ can be measured ex-situ for bigger ($\gtrsim 1\,\mu m$) dust grains. We note that we disregarded grain size for now, the density n represents the number density of *suitable* dust grains, whatever the suitability criteria are.

Since the Solar system near the ecliptic is our main goal, we will introduce assumptions on the shape of, and therefore simplifications to f:

- We assume that the plane $x \otimes y$ is going to be the ecliptic, with $(0, 0)$ point being the Sun and assume that all the mass of the distribution is situated in this plane, with no pole-ward component of the speed v_z.
- We assume that the dust cloud has a rotational symmetry around the z axis, and for convenience we are going to use the density $\tilde{f}$ expressed using (r, ϕ) instead of (x, y), where $r = \sqrt{x^2 + y^2}$ and ϕ is the angle of rotation around z-axis, measured from an arbitrary ray in the ecliptic.
- We assume the dust grains don't collide. Then we make use of Liouville's theorem on the space $(\mathbf{r}, \mathbf{v})$.

The first assumption is translated to f using degenerate distributions $\delta(\cdot)$ as

$$f(x, y, z, v_x, v_y, v_z) = f(x, y, 0, v_x, v_y, 0)\delta_0(z)\delta_0(v_z). \tag{A.3}$$

The second assumption is translated using r, ϕ as

$$
\begin{aligned}
& f(x, y, 0, v_x, v_y, 0)\delta_0(z)\delta_0(v_z) \\
=& f(r, 0, 0, v_x, v_y, 0)\delta_0(z)\delta_0(v_z) \\
=& \tilde{f}(r, 0, 0, v_x, v_y, 0)\delta_0(z)\delta_0(v_z) \\
=& \tilde{f}(r, \phi, 0, v_x, v_y, 0)\delta_0(z)\delta_0(v_z);\ \forall \phi \in \mathbb{R},
\end{aligned} \tag{A.4}
$$

where the first three arguments of f are all position arguments, where $\tilde{f}$ has a position, angle, and a position arguments. From now on, we will also use a more compact 4D distribution f, with the meaning

$$
\begin{aligned}
f(x, y, z, v_x, v_y, v_z) &= \tilde{f}(r, \phi, 0, v_r, v_\phi, 0)\delta_0(z)\delta_0(v_z) \\
&\equiv f(r, \phi, v_r, v_\phi)\delta_0(z)\delta_0(v_z).
\end{aligned} \tag{A.5}
$$

The third assumption has the form of

$$
\begin{aligned}
f(\mathbf{r}_1, \mathbf{v}_1) &= f(\mathbf{r}_2, \mathbf{v}_2) \Leftrightarrow \\
f(r_1, \phi_1, v_{r,1}, v_{\phi,1}) &= f(r_2, \phi_2, v_{r,2}, v_{\phi,2})
\end{aligned} \tag{A.6}
$$

provided that the points $(\mathbf{r}_1, \mathbf{v}_1), (\mathbf{r}_2, \mathbf{v}_2)$ (or, alternatively expressed points $(r_1, \phi_1, v_{r,1}, v_{\phi,1}), (r_2, \phi_2, v_{r,2}, v_{\phi,2})$) share the same trajectory of the system in the phase space. We note that we use velocity, not the momentum, which is justified, since we assume the mass conservation $dm/dt = 0$ for each particle. We assume the dust cloud is composed of bound dust grains, each of them on a heliocentric orbit. Then Eq. A.6 holds for any two points of

an orbit of a grain. If we assume all the grains follow the same gravity field with the effective gravitational parameter

$$\mu = (1 - \beta)\kappa M_{Sun}, \tag{A.7}$$

where β is the grain's radiation pressure to gravity ratio and κM_{Sun} is the solar gravitational parameter. Then all the grains which acquire the state of $(\mathbf{r}_1, \mathbf{v}_1)$ will also acquire the state of $(\mathbf{r}_2, \mathbf{v}_2)$, if this a valid solution for one of them. Therefore, we may study f in a convenient point of the orbit of our choice while being assured, it remains the same throughout the orbit.

Appendix A.2: Orbital mechanics

From A.6 we know that

$$f(r_{peri}, 0, 0, v_{peri}) = f(r, \phi, v_r, v_\phi), \tag{A.8}$$

provided that the spacecraft state in perihelion $(r_{peri}, 0, 0, v_{peri})$ shares the same orbit with a general state (r, ϕ, v_r, v_ϕ). By applying the laws of orbital motion, we are going to find the relationship between the points $(r_{peri}, 0, 0, v_{peri})$ and (r, ϕ, v_r, v_ϕ). We know the angular momentum is conserved:

$$r_{peri} v_{peri} = v_\phi r \Leftrightarrow v_{peri} = \frac{v_\phi r}{r_{peri}} \Leftrightarrow r_{peri} = \frac{v_\phi r}{v_{peri}}. \tag{A.9}$$

as well as the energy is:

$$v_{peri}^2 - \frac{2\mu}{r_{peri}} = v_\phi^2 + v_r^2 - \frac{2\mu}{r}. \tag{A.10}$$

Substituting v_{peri} from the angular momentum, we get

$$\left(\frac{v_\phi r}{r_{peri}}\right)^2 - \frac{2\mu}{r_{peri}} = v_\phi^2 + v_r^2 - \frac{2\mu}{r}, \tag{A.11}$$

and multiplying by r^2 we get

$$
\begin{aligned}
r_{peri}^2\left(v_\phi^2 + v_r^2 - \frac{2\mu}{r}\right) + r_{peri}(2\mu) - (v_\phi^2 r^2) &= 0 \\
a r_{peri}^2 + b r_{peri} + c &= 0.
\end{aligned} \tag{A.12}
$$

The two formal solutions of this equation are

$$r_{peri} = \frac{-b \pm \sqrt{b^2 - 4ac}}{2a}, \tag{A.13}$$

where $(+)$ and $(-)$ correspond to the aphelion and perihelion respectively, since we didn't assume anything other than a stationary point yet. Hence, $(-)$ corresponds to the true r_{peri} and substituting back for a, b, c and substituting for v_{peri} from Eq. A.9 we get:

$$
\begin{aligned}
r_{peri} &= \frac{-b - \sqrt{b^2 - 4ac}}{2a} = \frac{-\mu - \sqrt{\mu^2 + \left(v_\phi^2 + v_r^2 - \frac{2\mu}{r}\right)(v_\phi^2 r^2)}}{\left(v_\phi^2 + v_r^2 - \frac{2\mu}{r}\right)} \\
v_{peri} &= \frac{v_\phi r}{r_{peri}}.
\end{aligned} \tag{A.14}
$$

These two equations are what was needed to solve Eq. A.8. However, our goal is to study different eccentricities. Since an arbitrary distribution of eccentricities is straight-forward to approximate with a linear combination of sharp-eccentricity terms, we will now focus on a sharp eccentricity e. Assuming that all the

grains not only feel the same effective gravity μ, but they also have the same eccentricity e, it is apparent that *only one speed v_{peri} is allowed in the perihelion r_{peri}, which conforms to the eccentricity e* ($\star$). Vis-viva equation in perihelion gives

$$v_{peri} = \sqrt{\mu \frac{1+e}{r_{peri}}}. \qquad (A.15)$$

Substituting for v_{peri} from Eq. A.9, we get

$$\left(\frac{v_\phi r}{r_{peri}}\right)^2 = \mu \frac{1+e}{r_{peri}}$$

$$r_{peri} = \frac{v_\phi^2 r^2}{\mu(1+e)}. \qquad (A.16)$$

This equation is the bond between an arbitrary r, v_r, v_ϕ and the only corresponding r_{peri}, v_{peri} given the eccentricity e.

As a reasonable simplification (Giese et al. 1986), we assume the number density $n(x, y, z)$ in the ecliptic depends on the heliocentric distance:

$$n(x, y, z) = n(r, 0)\delta_0(z) = A\left(\frac{r}{r_0}\right)^\gamma \delta_0(z) = \delta_0(z)\frac{A}{r_0^\gamma}r^\gamma, \qquad (A.17)$$

where γ is a parameter, reasonably constrained by experiment. We normalized the expression by the number density at r_0, which might be for example 1 AU. Assume this dependence ($\propto r^\gamma$) holds for the distribution of dust grains in their perihelia (see section A.5 for the discussion), which is surely an acceptable assumption, at least for low e, since at low e, the difference between r_{peri} and r_{aph} is very small.

Appendix A.3: Velocity moments' integration

The flux measured in-situ with a probe in the point of (x, y) depends on the probe velocity and the volocities of the grains (v_x, v_y). Sine we WLOG assumed $x = r \Rightarrow y = 0 \Leftrightarrow \phi = 0$, we change the notation

$$(v_x, v_y) \mapsto (v_r, v_\phi), \qquad (A.18)$$

where $v_x = v_r$ is the radial dust speed and $v_y = v_\phi$ is the azimuthal dust speed, both in the unit of translational speed (as not to confuse with the angular speed $\dot\phi \neq v_\phi = r\dot\phi$). We are interested in the (in-situ) detection rate (flux), as measured with a probe. The net flux of particles through the x-plane is the first speed moment

$$j_x = \iiint_{\mathbb{R}^3} v_x f(\mathbf{r}, \mathbf{v}) \, dv_x \, dv_y \, dv_z. \qquad (A.19)$$

The SI unit is $[j_x] = m^{-2}s^{-1}$. We are however not interested in the net flux j_x but the total flux $j_{tot,x}$ onto the plane x. For the stationary plane x, we have

$$j_{tot,x} = \int_0^\infty \iint_{\mathbb{R}^2} v_x f(\mathbf{r}, \mathbf{v}) \, dv_x \, dv_y \, dv_z$$

$$+ \int_{-\infty}^0 \iint_{\mathbb{R}^2} -v_x f(\mathbf{r}, \mathbf{v}) \, dv_x \, dv_y \, dv_z. \qquad (A.20)$$

Should the probe be moving in $+x$-direction with the speed of $v_{p,x}$, the detected net flux is going to be

$$j_{tot,x} = \int_{v_{p,x}}^\infty \iint_{\mathbb{R}^2} (v_x - v_{p,x})f(\mathbf{r}, \mathbf{v}) \, dv_x \, dv_y \, dv_z$$

$$- \int_{-\infty}^{v_{p,x}} \iint_{\mathbb{R}^2} (v_x - v_{p,x})f(\mathbf{r}, \mathbf{v}) \, dv_x \, dv_y \, dv_z. \qquad (A.21)$$

Since we assumed all the dust being concentrated around the ecliptic plane (Eqs. A.3, A.5):

$$j_{tot,x} = \int_{v_{p,x}}^\infty \iint_{\mathbb{R}^2} (v_x - v_{p,x})f(r, \phi, v_r, v_\phi)\delta_0(z)\delta_0(v_z) \, dv_x \, dv_y \, dv_z$$

$$- \int_{-\infty}^{v_{p,x}} \iint_{\mathbb{R}^2} (v_x - v_{p,x})f(r, \phi, v_r, v_\phi)\delta_0(z)\delta_0(v_z) \, dv_x \, dv_y \, dv_z$$

$$= \delta_0(z) \int_{v_{p,x}}^\infty \int_{\mathbb{R}} (v_x - v_{p,x})f(r, \phi, v_r, v_\phi) \, dv_x \, dv_y$$

$$- \delta_0(z) \int_{-\infty}^{v_{p,x}} \int_{\mathbb{R}} (v_x - v_{p,x})f(r, \phi, v_r, v_\phi) \, dv_x \, dv_y. \qquad (A.22)$$

And since we align the x-axis with the probe, we might investigate the flux measured on radially oriented surfaces of the probe as

$$j_{tot,rad} = \delta_0(z) \int_{v_{p,rad}}^\infty \int_{\mathbb{R}} (v_r - v_{p,rad})f(r, 0, v_r, v_\phi) \, dv_r \, dv_\phi$$

$$- \delta_0(z) \int_{-\infty}^{v_{p,rad}} \int_{\mathbb{R}} (v_r - v_{p,rad})f(r, 0, v_r, v_\phi) \, dv_r \, dv_\phi, \qquad (A.23)$$

and, analogically, the flux measured on the azimuthally oriented surfaces as

$$j_{tot,azim} = \delta_0(z) \int_{\mathbb{R}} \int_{v_{p,azim}}^\infty (v_\phi - v_{p,azim})f(r, 0, v_r, v_\phi) \, dv_r \, dv_\phi$$

$$- \delta_0(z) \int_{\mathbb{R}} \int_{-\infty}^{v_{p,azim}} (v_\phi - v_{p,azim})f(r, 0, v_r, v_\phi) \, dv_r \, dv_\phi, \qquad (A.24)$$

where $v_{p.azim}$ is the azimuthal speed of the probe (prograde, locally in +y-direction).

To obtain the most convenient form of f in an easily integrable shape, we use two additional pieces of information: 1. the dependence on the heliocentric distance (Eq. A.17), and 2. the fact, that Eqs. A.16 and A.14 must be demanded consistent, which is the equivalent to the ($\star$) claim. We are shortly going to integrate f over v_r and v_ϕ, as in Eqs. A.23 and A.24. We know that not all combinations of v_r, v_ϕ are possible given r, e. Instead of integrating in two dimensions, we will integrate in $v_r \otimes v_\phi$ space along the path $v_r(v_\phi)$ given by ($\star$). Hence, we relate Eqs. A.16 and A.14 with the goal of obtaining $v_r(v_\phi)$:

$$\frac{-\mu - \sqrt{\mu^2 + \left(v_\phi^2 + v_r^2 - \frac{2\mu}{r}\right)(v_\phi^2 r^2)}}{\left(v_\phi^2 + v_r^2 - \frac{2\mu}{r}\right)} = \frac{v_\phi^2 r^2}{\mu(1+e)} \qquad (A.25)$$

This quadratic equation has two solutions for v_r:

$$v_r = \pm \frac{\sqrt{(e^2 - 1)\mu^2 + 2\mu v_\phi^2 r - v_\phi^4 r^2}}{v_\phi r} = \pm \tilde{v}, \qquad (A.26)$$

These solutions correspond to the radial speeds of pre-perihelion (in-going, $v_r < 0$) and post-perihelion (out-going, $v_r > 0$) dust, as at a given r and with a given v_ϕ. Since f of the dust cloud is assumed stationary, the grains don´t collide and are in repetitive orbits, therefore there are exactly as many in-going as out-going.

Now to get a convenient shape of f:

$$f(r, 0, v_r, v_\phi) = f(r, 0, v_\phi)\delta(v_r \pm \tilde{v})$$

$$\propto r^\gamma \hat{f}(v_\phi)\delta(v_r \pm \tilde{v}), \qquad (A.27)$$

where in the first step we expressed the condition A.26 and newly used a 3D distribution f according to $f(r, \phi, v_\phi)\delta(v_r \pm \tilde{v}) = f(r, \phi, v_r, v_\phi)$ and in the second step we expressed the condition that $n(r) \propto r^\gamma$ using a new 1D $\hat{f}(v_\phi)$ and we lost the normalization. Since Liouville's theorem says that the density is the same along the trajectory of the grain, it is the same in perihelion as well, and its moments are the same, and therefore integrating over z, v_z, v_r in an arbitrary time (LHS) and in perihelion (RHS):

$$r^\gamma \hat{f}(v_\phi) = r^\gamma_{peri}\hat{f}(v_{peri})$$

$$r^\gamma \hat{f}(v_\phi) = \left(\frac{v_\phi^2 r^2}{\mu(1+e)}\right)^\gamma \hat{f}\left(\frac{\mu(1+e)}{v_\phi r}\right)$$

$$r^\gamma \hat{f}(v_\phi) = (\mu(1+e))^{-\gamma} v_\phi^{2\gamma} r^{2\gamma} \hat{f}\left(\frac{\mu(1+e)}{v_\phi r}\right). \tag{A.28}$$

Since $\mu(1+e)$ is a plain number, and except for $\hat{f}(\dots)$ we only have r^{c_1} and $v_\phi^{c_2}$ and we demand the equality for arbitrary r, v_ϕ, the only thinkable solution for f is of the form

$$\hat{f}(x) = Cx^b, \tag{A.29}$$

therefore:

$$r^\gamma C v_\phi^b = (\mu(1+e))^{-\gamma} v_\phi^{2\gamma} r^{2\gamma} C\left(\frac{\mu(1+e)}{v_\phi r}\right)^b$$

$$1 = (\mu(1+e))^{b-\gamma} v_\phi^{2\gamma-2b} r^{\gamma-b}$$

$$1 = \left(\frac{v_\phi^2 r}{\mu(1+e)}\right)^{\gamma-b}, \tag{A.30}$$

Where the only suitable solution is $b = \gamma$. Therefore, $\hat{f}(x) = Cx^\gamma$ Eq. A.27 with Eq. A.26 give:

$$f(r, 0, v_r, v_\phi) =$$
$$= C \cdot (rv_\phi)^\gamma \delta(z)\delta(v_z)\delta(v_r \pm \tilde{v})$$
$$= C \cdot (rv_\phi)^\gamma \delta(z)\delta(v_z)\delta\left(v_r \pm \frac{\sqrt{(e^2-1)\mu^2 + 2\mu v_\phi^2 r - v_\phi^4 r^2}}{v_\phi r}\right). \tag{A.31}$$

The last parenthesis of this equation may be interpreted as the integration trajectory in the $v_r \otimes v_\phi$ space. Since our integration parameter of the contraction from the the $v_r \otimes v_\phi$ space to a 1D space of the path is going to be v_ϕ, we need the integration boundaries for v_ϕ. The integration boundaries are given by the lowermost and the uppermost v_ϕ the probe may encounter, given r,e. The lowest possible v_ϕ corresponds to the probe being in aphelion, whereas the highest corresponds to it being in the perihelion. We use Eq. A.26, and both in the perihelion and in the aphelion, we get $v_r = 0$, hence

$$(e^2 - 1)\mu^2 + 2\mu v_\phi^2 r - v_\phi^4 r^2 = 0, \tag{A.32}$$

and this quadratic equation in v_ϕ^2 has two solutions:

$$v_\phi^2 = \frac{(1 \pm e)\mu}{r}, \tag{A.33}$$

corresponding to the highest possible v_ϕ (in the case r is the perihelion) and the lowest possible (in the case r is the aphelion). Negative v_ϕ would correspond to the dust grains on retrograde orbits and are disregarded as we only want to include prograde dust grains for now. These are, therefore, our integration boundaries:

$$\sqrt{\frac{(1-e)\mu}{r}} < v_\phi < \sqrt{\frac{(1+e)\mu}{r}}. \tag{A.34}$$

We note that these correspond to the degenerate solutions of Eq. A.26, which makes sense, since Eq. A.26 defines a cyclic trajectory in the $v_r \otimes v_\phi$ space.

Radial flux

$$j_{tot,rad} = \delta(z)\int_{v_{p,rad}}^\infty \int_\mathbb{R} (v_r - v_{p,rad})f(r, 0, v_r, v_\phi)\, dv_r\, dv_\phi$$
$$\quad - \delta(z)\int_{-\infty}^{v_{p,rad}} \int_\mathbb{R} (v_r - v_{p,rad})f(r, 0, v_r, v_\phi)\, dv_r\, dv_\phi$$
$$= \delta(z)Cr^\gamma \int_{v_{p,rad}}^\infty \int_\mathbb{R} (v_r - v_{p,rad})v_\phi^\gamma \delta(v_r \pm \tilde{v})\, dv_r\, dv_\phi$$
$$\quad - \delta(z)Cr^\gamma \int_{-\infty}^{v_{p,rad}} \int_\mathbb{R} (v_r - v_{p,rad})v_\phi^\gamma \delta(v_r \pm \tilde{v})\, dv_r\, dv_\phi. \tag{A.35}$$

The expression contains two terms: $j_{tot,rad} = \delta_0(z)Cr^\gamma(j_{rad}^+ - j_{rad}^-)$, which have the boundaries $v_r > v_{p,rad}$ and $v_{p,rad} > v_r$ respectively, which corresponds to flux on the front-side (sun-facing, $+$) and on the back-side ($-$) respectively. We translate these boundaries from v_r to v_ϕ in order to integrate over the parameter v_ϕ using the Heaviside function. Each of these two has two variants: post-perihelion (*post*, $v_r > 0$) and pre-perihelion (*pre*, $v_r < 0$) dust, as $\pm \tilde{v}$ in Eq. A.26. Thus, we get four integral terms, each with a prefactor of $1/2$:

$$j_{rad}^{+,pre} = \frac{1}{2}\int_{v_{p,rad}}^\infty \int_\mathbb{R} (v_r - v_{p,rad})v_\phi^\gamma \delta(v_r + \tilde{v})\, dv_r\, dv_\phi$$
$$= \frac{1}{2}\int_\mathbb{R} \int_\mathbb{R} (v_r - v_{p,rad})v_\phi^\gamma \delta(v_r + \tilde{v})H(v_r - v_{p,rad})\, dv_r\, dv_\phi$$
$$= \frac{1}{2}\int_\mathbb{R} (-\tilde{v} - v_{p,rad})v_\phi^\gamma H(-\tilde{v} - v_{p,rad})\, dv_\phi$$
$$= \frac{1}{2}\int_{\sqrt{\frac{(1-e)\mu}{r}}}^{\sqrt{\frac{(1+e)\mu}{r}}} (-\tilde{v} - v_{p,rad})v_\phi^\gamma H(-\tilde{v} - v_{p,rad})\, dv_\phi, \tag{A.36}$$

$$j_{rad}^{+,post} = \frac{1}{2}\int_{v_{p,rad}}^\infty \int_\mathbb{R} (v_r - v_{p,rad})v_\phi^\gamma \delta(v_r - \tilde{v})\, dv_r\, dv_\phi$$
$$= \frac{1}{2}\int_{\sqrt{\frac{(1-e)\mu}{r}}}^{\sqrt{\frac{(1+e)\mu}{r}}} (\tilde{v} - v_{p,rad})v_\phi^\gamma H(\tilde{v} - v_{p,rad})\, dv_\phi, \tag{A.37}$$

$$j_{rad}^{-,pre} = \frac{1}{2}\int_{-\infty}^{v_{p,rad}} \int_\mathbb{R} (v_r - v_{p,rad})v_\phi^\gamma \delta(v_r + \tilde{v})\, dv_r\, dv_\phi$$
$$= \frac{1}{2}\int_{\sqrt{\frac{(1-e)\mu}{r}}}^{\sqrt{\frac{(1+e)\mu}{r}}} (-\tilde{v} - v_{p,rad})v_\phi^\gamma H(\tilde{v} + v_{p,rad})\, dv_\phi, \tag{A.38}$$

$$j_{rad}^{-,post} = \frac{1}{2}\int_{-\infty}^{v_{p,rad}} \int_\mathbb{R} (v_r - v_{p,rad})v_\phi^\gamma \delta(v_r - \tilde{v})\, dv_r\, dv_\phi$$
$$= \frac{1}{2}\int_{\sqrt{\frac{(1-e)\mu}{r}}}^{\sqrt{\frac{(1+e)\mu}{r}}} (\tilde{v} - v_{p,rad})v_\phi^\gamma H(-\tilde{v} + v_{p,rad})\, dv_\phi, \tag{A.39}$$

where

$$\tilde{v} = \frac{\sqrt{(e^2 - 1)\mu^2 + 2\mu v_\phi^2 r - v_\phi^4 r^2}}{v_\phi r}, \tag{A.40}$$

and altogether:

$$j_{tot,rad} = C\delta_0(z)r^\gamma \left(j_{rad}^{+,pre} + j_{rad}^{+,post} - j_{rad}^{-,pre} - j_{rad}^{-,post} \right). \tag{A.41}$$

We note that even and odd terms are straightforward to join as the only difference is the complementary Heaviside, but in the present shape it is easy to account for different effective areas from front and from the back of the probe in this function, since front and back terms are separated. Evaluate this by MC.

Azimuthal flux

$$
\begin{aligned}
j_{tot,azim} = {} & \delta(z) \int_\mathbb{R} \int_{v_{p,azim}}^\infty (v_\phi - v_{p,azim}) f(r, 0, v_r, v_\phi)\, dv_r\, dv_\phi \\
& - \delta(z) \int_\mathbb{R} \int_{-\infty}^{v_{p,azim}} (v_\phi - v_{p,azim}) f(r, 0, v_r, v_\phi)\, dv_r\, dv_\phi, \\
= {} & \delta(z)Cr^\gamma \int_\mathbb{R} \int_{v_{p,azim}}^\infty (v_\phi - v_{p,azim}) v_\phi^\gamma \delta(v_r \pm \tilde{v})\, dv_r\, dv_\phi \\
& - \delta(z)Cr^\gamma \int_\mathbb{R} \int_{-\infty}^{v_{p,azim}} (v_\phi - v_{p,azim}) v_\phi^\gamma \delta(v_r \pm \tilde{v})\, dv_r\, dv_\phi
\end{aligned}
\tag{A.42}
$$

The expression contains two terms: $j_{tot,azim} = \delta(z)Cr^\gamma(j_{azim}^+ - j_{azim}^-)$, which have the boundaries $v_\phi > v_{p,azim}$ and $v_{p,azim} > v_\phi$ respectively. Since we assume prograde dust only ($v_\phi > 0$), and pre-perihelion and post-perihelion have the same effect on the azimuthal flux, there is no further multiplication of terms, as in the case of radial flux.

$$
\begin{aligned}
j_{azim}^+ = {} & \int_\mathbb{R} \int_{v_{p,azim}}^\infty (v_\phi - v_{p,azim}) v_\phi^\gamma \delta(v_r \pm \tilde{v})\, dv_r\, dv_\phi \\
= {} & \int_{v_{p,azim}}^\infty (v_\phi - v_{p,azim}) v_\phi^\gamma\, dv_\phi \\
= {} & \int_{\max\left[\sqrt{\frac{(1-e)\mu}{r}}, v_{p,azim}\right]}^{\max\left[\sqrt{\frac{(1+e)\mu}{r}}, v_{p,azim}\right]} (v_\phi - v_{p,azim}) v_\phi^\gamma\, dv_\phi \\
= {} & \left[\frac{v_\phi^{\gamma+2}}{\gamma + 2} - \frac{v_\phi^{\gamma+1} v_{p,azim}}{\gamma + 1} \right]_{\max\left[\sqrt{\frac{(1-e)\mu}{r}}, v_{p,azim}\right]}^{\max\left[\sqrt{\frac{(1+e)\mu}{r}}, v_{p,azim}\right]},
\end{aligned}
\tag{A.43}
$$

$$
\begin{aligned}
j_{azim}^- = {} & \int_\mathbb{R} \int_{-\infty}^{v_{p,azim}} (v_\phi - v_{p,azim}) v_\phi^\gamma \delta(v_r \pm \tilde{v})\, dv_r\, dv_\phi \\
= {} & \int_{-\infty}^{v_{p,azim}} (v_\phi - v_{p,azim}) v_\phi^\gamma\, dv_\phi \\
= {} & \int_{\min\left[\sqrt{\frac{(1-e)\mu}{r}}, v_{p,azim}\right]}^{\min\left[\sqrt{\frac{(1+e)\mu}{r}}, v_{p,azim}\right]} (v_\phi - v_{p,azim}) v_\phi^\gamma\, dv_\phi \\
= {} & \left[\frac{v_\phi^{\gamma+2}}{\gamma + 2} - \frac{v_\phi^{\gamma+1} v_{p,azim}}{\gamma + 1} \right]_{\min\left[\sqrt{\frac{(1-e)\mu}{r}}, v_{p,azim}\right]}^{\min\left[\sqrt{\frac{(1+e)\mu}{r}}, v_{p,azim}\right]},
\end{aligned}
\tag{A.44}
$$

where we very liberally ignred $\delta_0(v_r \pm \dots)$, but since we integrate in v_r over $\mathbb{R}$, it doesn't matter where exactly this mass is accounted for. Altogether we have:

$$j_{tot,azim} = \delta(z)Cr^\gamma(j_{azim}^+ - j_{azim}^-), \tag{A.45}$$

which is easy and straightforward to evaluate. Finally,

$$j_{tot} = j_{tot,azim} + j_{tot,rad}. \tag{A.46}$$

Appendix A.4: Normalization

In order to normalize the flux properly to a known value of density at 1 AU in the unit of m^{-3}, we need to evaluate the number density at r_0, which might conveniently be 1 AU. If we don't do that, then Eqs. A.36 - A.39, A.43, A.44 all vary as $\propto 2\sqrt{e}$ for low e. Let's evaluate $n(r = r_0)$ for the parameter e. Analogically to Eqs. A.41 and A.45:

$$
\begin{aligned}
n = {} & \delta(z) \int_\mathbb{R} \int_\mathbb{R} f(r, 0, v_r, v_\phi)\, dv_r\, dv_\phi, \\
= {} & \delta(z)Cr_0^\gamma \int_\mathbb{R} \int_\mathbb{R} v_\phi^\gamma \delta(v_r \pm \tilde{v})\, dv_r\, dv_\phi \\
= {} & \delta(z)Cr_0^\gamma \int_{\sqrt{\frac{(1-e)\mu}{r_0}}}^{\sqrt{\frac{(1+e)\mu}{r_0}}} v_\phi^\gamma\, dv_\phi \\
= {} & \delta(z)Cr_0^\gamma \left[\frac{v_\phi^{\gamma+1}}{\gamma + 1} \right]_{\sqrt{\frac{(1-e)\mu}{r_0}}}^{\sqrt{\frac{(1+e)\mu}{r_0}}} \\
= {} & \delta(z)Cr_0^\gamma \frac{1}{\gamma + 1} \left[v_\phi^{\gamma+1} \right]_{\sqrt{\frac{(1-e)\mu}{r_0}}}^{\sqrt{\frac{(1+e)\mu}{r_0}}} \\
= {} & \delta(z)Cr_0^\gamma \frac{1}{\gamma + 1} \left(\left(\frac{(1+e)\mu}{r_0}\right)^{\frac{\gamma+1}{2}} - \left(\frac{(1-e)\mu}{r_0}\right)^{\frac{\gamma+1}{2}} \right) \\
= {} & \delta(z)Cr_0^\gamma \frac{1}{\gamma + 1} \left(\frac{\mu}{r_0}\right)^{\frac{\gamma+1}{2}} \left((1+e)^{\frac{\gamma+1}{2}} - (1-e)^{\frac{\gamma+1}{2}} \right)
\end{aligned}
\tag{A.47}
$$

Thus, we get that:

$$\delta_0(z)C = \frac{n}{r_0^\gamma} \left(\frac{r_0}{\mu}\right)^{\frac{\gamma+1}{2}} \frac{(\gamma + 1)}{\left((1+e)^{\frac{\gamma+1}{2}} - (1-e)^{\frac{\gamma+1}{2}}\right)}, \tag{A.48}$$

where $[n] = m^{-3}$ at the distance of r_0.

Appendix A.5: Number density assumption

To derive the fluxes following the assumption of number density scaling as $n \propto r^\gamma$, we conveniently assumed the equivalence

$$n \propto r^\gamma \Leftrightarrow n \propto r_{peri}^\gamma. \tag{A.49}$$

Here we demonstrate the validity of this assumption. Assume a dust grain is in orbit with the perihelion r_{peri} and aphelion

$$r_{aph} = \frac{1+e}{1-e} r_{peri}, \tag{A.50}$$

where e is the eccentricity. The grain therefore spends time at the heliocentric distance r:

$$r_{peri} < r < r_{aph}, \tag{A.51}$$

and the time spent, and therefore the probability $f(r)$ the grain will be (in random time) found at r it spends at r is proportional to the magnitude of the radial speed $|v_r|$:

$$f(r|r_{peri}) \propto |v_r|(r) = \left| \frac{dr}{dt}(r) \right| = \sqrt{v^2 - v_\phi^2}, \tag{A.52}$$

where v and v_ϕ are the total and azimuthal speeds of the grain. Then we have from vis-viva equation:

$$v^2 = \mu \left(\frac{2}{r} - \frac{1}{a} \right) = \mu \left(\frac{2}{r} - \frac{1-e}{r_{peri}} \right), \tag{A.53}$$

and v_ϕ is obtained using momentum conservation as

$$v_\phi = \frac{v_{peri} r_{peri}}{r}, \tag{A.54}$$

where the perihelion speed v_{peri} is also obtained from vis-viva as

$$v_{peri} = \sqrt{\mu \frac{1+e}{r_{peri}}}, \tag{A.55}$$

which altogether gives:

$$
\begin{aligned}
f(r|r_{peri}) \propto |v_r|(r) &= \sqrt{\mu \left(\frac{2}{r} - \frac{1-e}{r_{peri}} \right) - \left(\frac{\sqrt{\mu \frac{1+e}{r_{peri}}} r_{peri}}{r} \right)^2} \\
&= \sqrt{\mu \left(\frac{2}{r} - \frac{1-e}{r_{peri}} - \frac{(1+e)r_{peri}}{r^2} \right)} \\
&= \sqrt{\frac{2\mu}{r} \left(1 - \left(\frac{(1-e)}{2} \frac{r}{r_{peri}} + \frac{(1+e)}{2} \frac{r_{peri}}{r} \right) \right)}.
\end{aligned}
\tag{A.56}
$$

Obtaining r from r_{peri} is a random process governed by the probability density function $f(r|r_{peri})$. We can therefore draw a sample of r_{peri} according to $f(r_{peri})$ and transform r_{peri} to r using the density $f(r|r_{peri})$ deriver here. As is shown in Fig. A.1, the dependence $n \propto r^\gamma$ is really obtained, if $n \propto r_{peri}^\gamma$ is assumed.
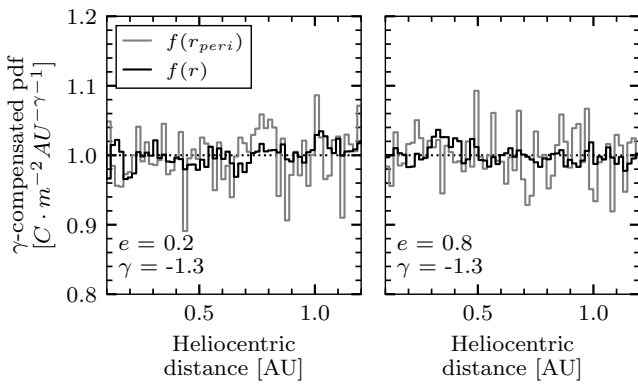

Fig. A.1: A sample of r_{peri} is drawn according to $n \propto r_{peri}^\gamma$ and transformed using $f(r|r_{peri})$. The distribution shows $n \propto r^\gamma$.

Appendix A.6: Generalization

Already included parameters The integrals for flux $j_{tot,rad}$ and $j_{tot,azim}$ as derived and expressed in Sec. A.3 already allow for evaluation of the flux along a trajectory of a spacecraft, given the eccentricity of the dust's orbits e, radiation pressure to gravity ratio β, distance-scaling parameter γ and cuboid-approximated spacecraft areas, since the flux is evaluated for each of the relevant spacecraft sides independently.

Retrograde grains The simplest addition is the fraction of retrograde grains in the dust cloud. Until, now all the dust grains were considered prograde, but the fraction of retrograde dust is taken into account by weighted summing of the flux encountered along the true spacecraft trajectory, with the flux encountered by mirrored (retrograde) spacecraft trajectory.

Higher exponent of the relative speed If the flux is assumed proportional to an exponent of velocity ϵ other than unity, this is taken into account by evaluating the higher moment of $(v_r - v_{p,rad})$ and $(v_\phi - v_{p,azim})$ in the terms of Eqs. A.41 and A.45 respectively, which is straight forward. We note that the normalization needs to be adjusted in this case as well, as a scale relative velocity v_0 has to be introduced, at which the number density is measured.

Inclination A single inclination angle θ different from zero can be introduced, under the assumption that all the grains share the same inclination, albeit in different orbital planes. Under this assumption, a spacecraft in the ecliptics can only encounter dust grains of this given inclination θ. Given it is PSP, which is of main interest, it is reasonable to approximate the spacecraft by a cyllinder, rather than a cuboid. This makes no difference, until $\theta \neq 0$ is examined.

We note that an arbitrary inclination of the orbital plane of each of the grains does not play a role in $j_{tot,rad}$. For the azimuthal component, we need to evaluate the moment $|v_\phi - v_{p,azim}|$ over the f, as a function of inclination θ. We assume the cyllindrical symmetry:

$$v_{cyl}(v_\phi) \equiv |v_\phi - v_{p,azim}| = \sqrt{v_{p,azim}^2 \sin^2 \theta + \left(v_\phi - v_{p,azim} \cos \theta \right)^2}, \tag{A.57}$$

which we then need to integrate to

$$j_{tot,azim} = \delta(z) C r^\gamma (j_{azim}^+ - j_{azim}^-), \tag{A.58}$$

where

$$j_{azim}^+ = \int_{\sqrt{\frac{(1-e)\mu}{r}}}^{\sqrt{\frac{(1+e)\mu}{r}}} v_{cyl}(v_\phi) v_\phi^\gamma H\left(v_{cyl}(v_\phi) \right) dv_\phi, \tag{A.59}$$

$$j_{azim}^- = \int_{\sqrt{\frac{(1-e)\mu}{r}}}^{\sqrt{\frac{(1+e)\mu}{r}}} v_{cyl}(v_\phi) v_\phi^\gamma H\left(-v_{cyl}(v_\phi) \right) dv_\phi. \tag{A.60}$$

Since by definition $\sqrt{\cdot} > 0$:

$$j_{azim}^+ - j_{azim}^- = \int_{\sqrt{\frac{(1-e)\mu}{r}}}^{\sqrt{\frac{(1+e)\mu}{r}}} v_{cyl}(v_\phi) v_\phi^\gamma dv_\phi, \tag{A.61}$$

which we evaluate easily by MC.

Table B.1: The representative orbital parameters for PSP's encounter groups.

Encounter group	Perihelion distance [Gm]	Perihelion speed [km/s]
1	24.8	95
2	19.4	109
3	14.2	127
4	11.1	147
5	9.2	163

We note that both non-zero eccentricity and non-zero inclination make the assumption of non-interacting grains problematic, but the collisional evolution of the dust cloud is beyond the scope of this work, and taken care of in reality by the micrometer dust cloud being constantly replenished by the product of collision of bigger grains.

Appendix B: Model trajectories of PSP

Every PSP's solar encounter is different from the previous one, even within the same orbital group. This is solely because of the motion of the Sun, which in the first approximation orbits around the common barycenter of the Sun — Jupiter system, which lies outside of the solar photosphere. PSP orbits the Sun on an orbit with perihelion distance sufficiently close the the Sun, so that this effect plays a role when the distance from the Sun is critical. This is however not as consequential as to change the results presented in this work. To get rid of the effect, we study fictitious, simplified solar encounters, which are assumed to lie in the ecliptic plane ($z = 0$) and which represent the actual ones well. The parameters of the encounters which we use for the present study are listen in Tab. B.1.

Appendix C: The flux slope scaling with orbital parameters

In Sec. 2, we claimed that the parameters: $e; \theta; \beta; rp$ all act to make the slope of flux steeper, when their values differ from the base case. Their influence is independently shown in Figs. C.1 – C.4.

Appendix D: The near-perihelia flux dependence on other parameters

In Sec. 3, we claimed that the parameters: $e; \theta; \beta; \gamma, rp$ do not change the location of the flux maxima appreciably. They however change the magnitude of the near-perihelia dip, especially the parameter e does. Their influence is independently shown in Figs. D.1 – D.5.
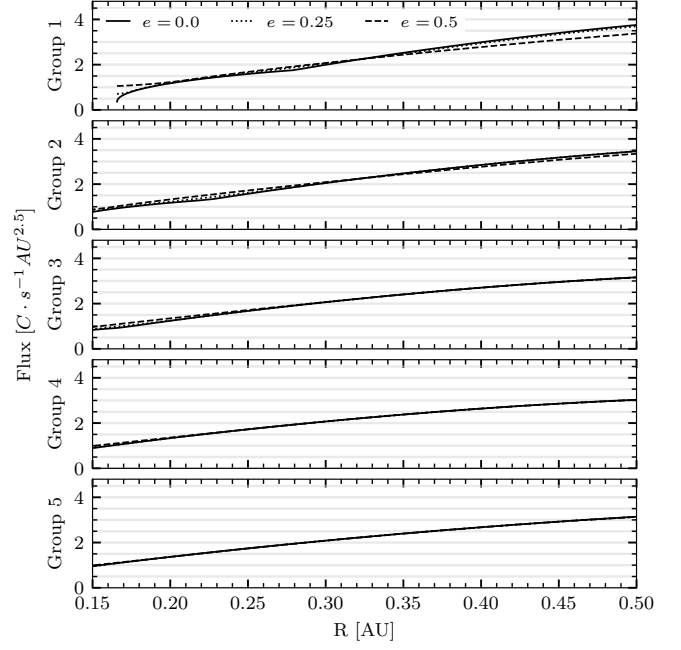

Fig. C.1: The base model-predicted flux is shown in the solid line. In addition, the influence of eccentricity on the slope is demonstrated.
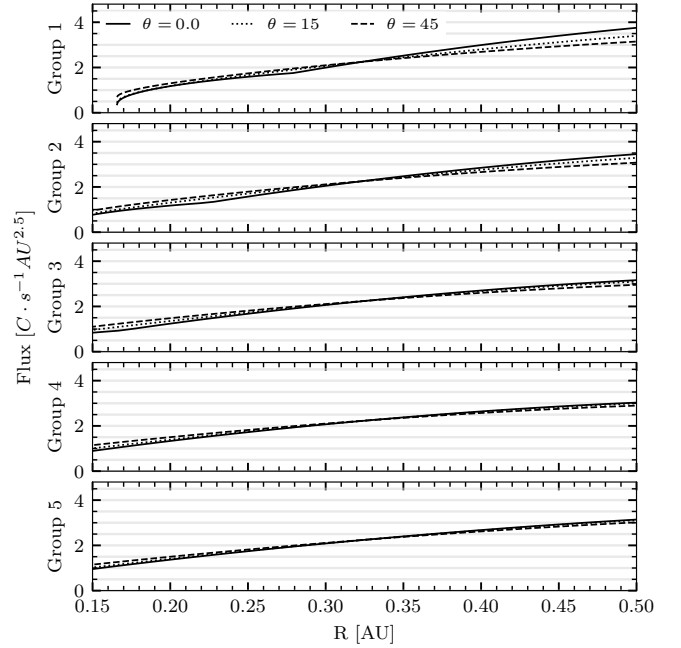

Fig. C.2: The base model-predicted flux is shown in the solid line. In addition, the influence of inclination on the slope is demonstrated.
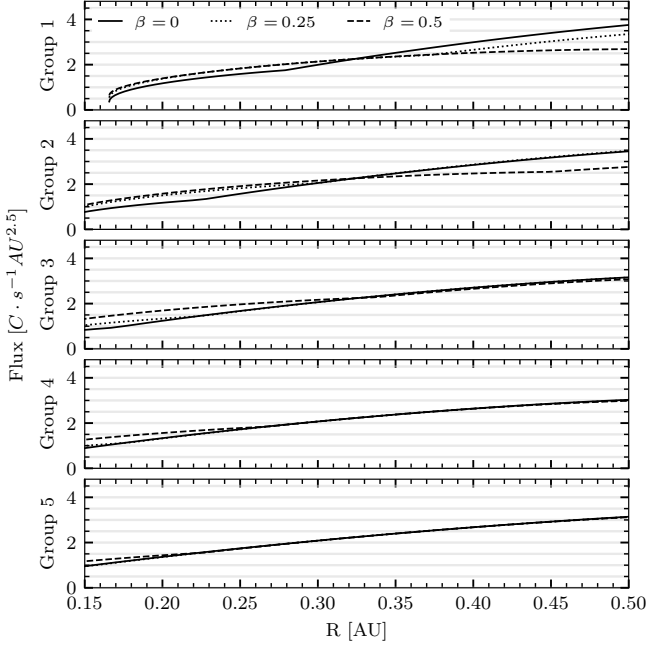
Fig. C.3: The base model-predicted flux is shown in the solid line. In addition, the influence of β value on the slope is demonstrated.

Fig. D.1: The base model-predicted flux is shown in the solid line. In addition, the influence of eccentricity on the slope is demonstrated.
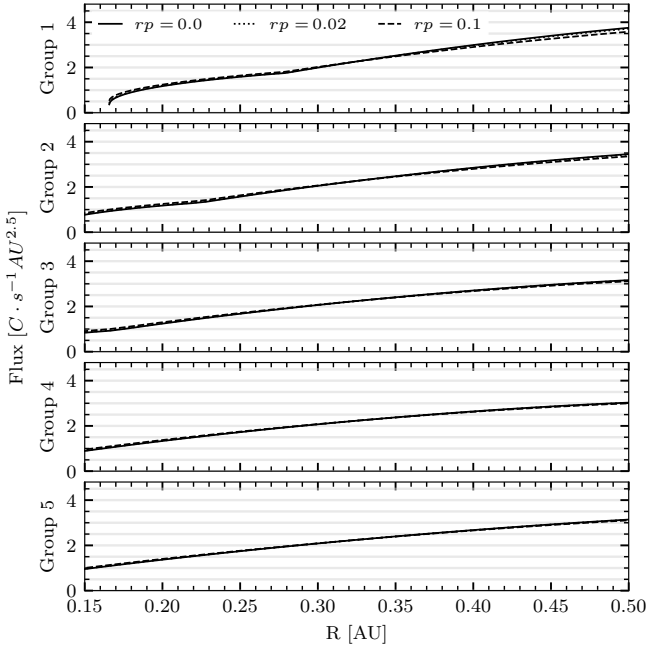

Fig. C.4: The base model-predicted flux is shown in the solid line. In addition, the influence of retrograde fraction on the slope is demonstrated.
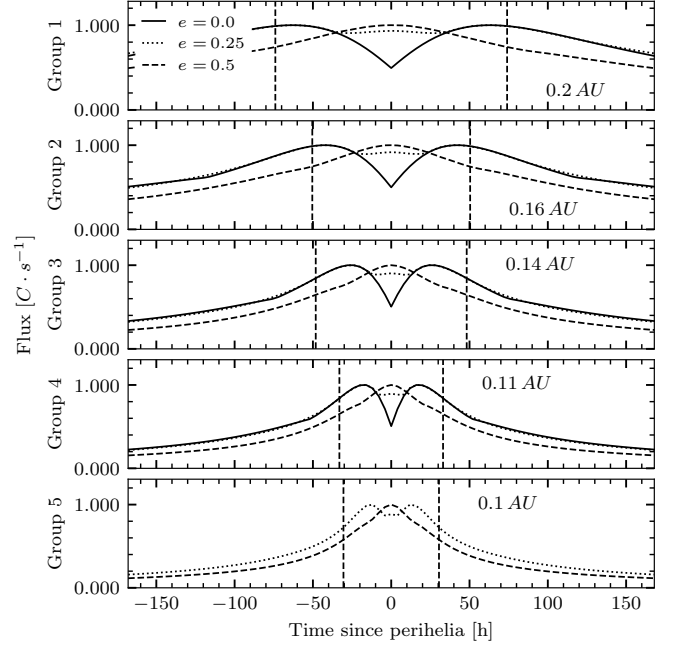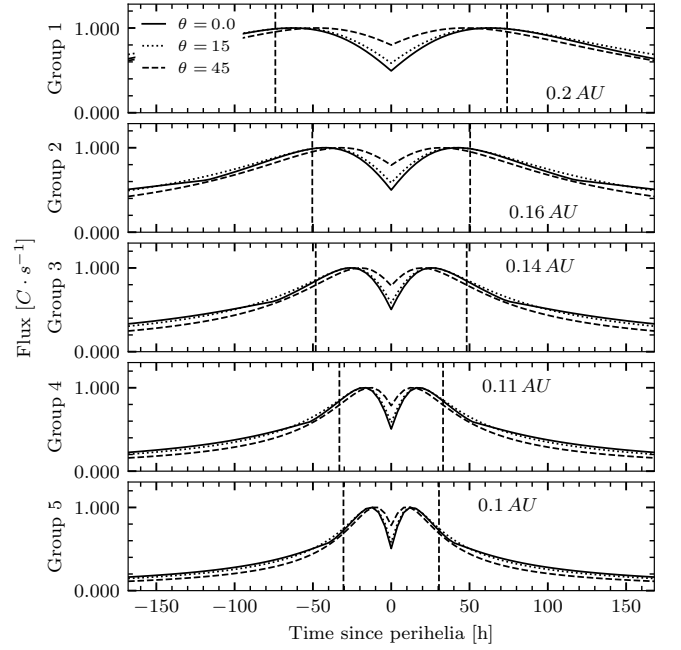

Fig. D.2: The base model-predicted flux is shown in the solid line. In addition, the influence of inclination is shown.
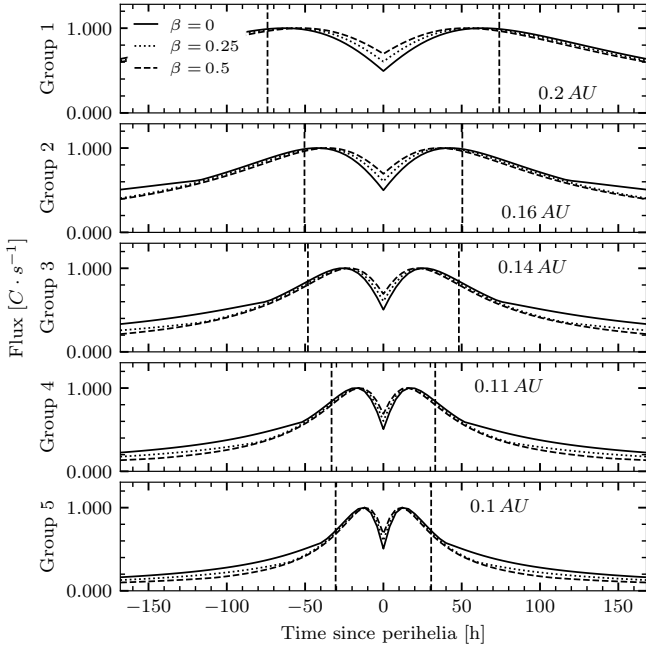
Fig. D.3: The base model-predicted flux is shown in the solid line. In addition, the influence of β value is shown.
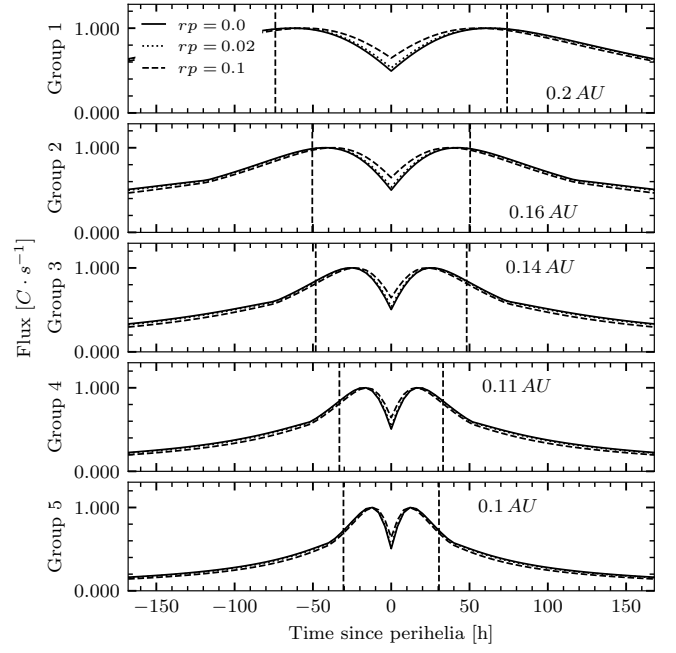
Fig. D.5: The base model-predicted flux is shown in the solid line. In addition, the influence of retrograde fraction is shown.
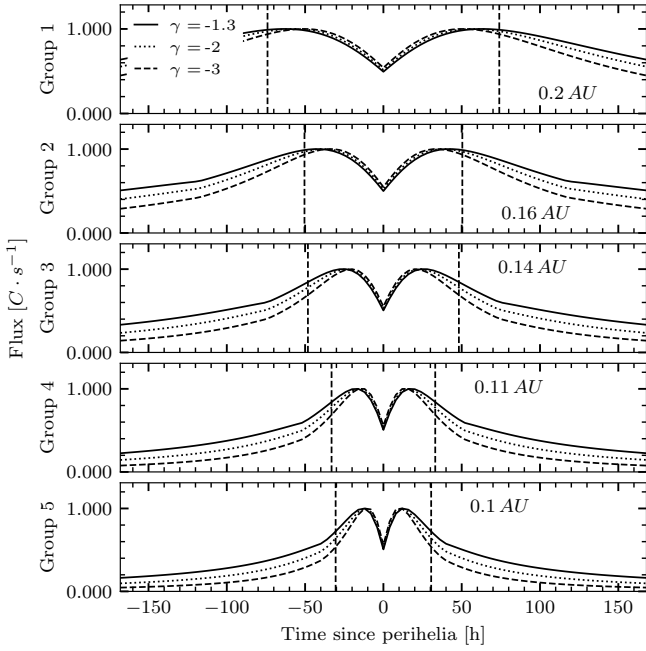

Fig. D.4: The base model-predicted flux is shown in the solid line. In addition, the influence of the spatial density scaling with heliocentric distance γ is shown.